JAIST Repository
https://dspace.jaist.ac.jp/

Title	Palladium Nanoparticles Combined with Reduced Graphene Oxide and Multiwall Carbon Nanotubes for Alkaline Ascorbic Acid Oxidation
Author(s)	Hasan, Md. Mahmudul; Li, Zhongping; Nagao, Yuki
Citation	Japanese Journal of Applied Physics, 62: 027003
Issue Date	2023-02-17
Type	Journal Article
Text version	author
URL	http://hdl.handle.net/10119/18809
Rights	This is the author's version of the work. It is posted here by permission of The Japan Society of Applied Physics. Copyright (C) 2023 The Japan Society of Applied Physics. Md. Mahmudul Hasan, Zhongping Li, Yuki Nagao, Japanese Journal of Applied Physics, 62, 2023, 027003. https://doi.org/10.35848/1347-4065/acb897
Description	

JAIST
JAPAN
ADVANCED INSTITUTE OF
SCIENCE AND TECHNOLOGY

Japan Advanced Institute of Science and Technology

Palladium Nanoparticles Combined with Reduced Graphene Oxide and Multiwall Carbon Nanotubes for Alkaline Ascorbic Acid Oxidation

Md. Mahmudul Hasan,[1] Zhongping Li,[1] Yuki Nagao,[1,*]

[1]*School of Materials Science, Japan Advanced Institute of Science and Technology, 1-1 Asahidai, Nomi, Ishikawa 923-1292, Japan.*

E-mail: ynagao@jaist.ac.jp

Ascorbic acid (vitamin C) is recognized as a viable alternative fuel for alkaline direct liquid fuel cells (DLFCs). After the potential anode catalyst was prepared by incorporating palladium nanoparticles (Pd NPs) into reduced graphene oxide (rGO) and multiwall carbon nanotube (MWCNT) hybrid nanocomposite (Pd/rGO/MWCNT) through a chemical reduction method, it was applied for electrooxidation of ascorbic acid (AA) in the alkaline condition. For AA electrooxidation, the Pd/rGO/MWCNT modified glassy carbon electrode (Pd/rGO/MWCNT/GCE) exhibited the highest current density of 5.18 mA cm^{-2}: much higher than a bare glassy carbon electrode (0.6 mA cm^{-2}). The Pd/rGO/MWCNT/GCE also demonstrated excellent stability for AA oxidation in the alkaline condition.

1. Introduction

The increased demand for energy along with the widespread use of fossil fuels has put enormous strain on the world's natural resources and caused global climate change. Scientists have recently shown interest in electrochemical energy storage and conversion devices to address climate change.[1)–6)] Fuel cells have been recognized as a possible alternative zero-emission energy conversion device.[7)–10)] Safety, environmental, and storage issues remain challenging for fuel cells such as borohydride fuel cells, hydrazine fuel cells, alcohol-based fuel cells, and hydrogen fuel cells.[11)–14)] Ascorbic acid (AA), a potential environmentally benign fuel for direct liquid fuel cells (DLFCs), is naturally abundant and produces nontoxic byproducts.[15)–19)] During electrochemical oxidation, AA releases two electrons and two protons.[20),21)] One can reasonably expect that DLFC

performance can be enhanced by the development of a more efficient electrocatalyst for AA electrooxidation.

Carbon-based materials have attracted great interest in the field of electrocatalysis because of their unique physical and chemical characteristics.[22),23)] Carbon electrodes are readily renewable and provide several benefits including ease of preparation, high stability, repeatability, and strong conductivity.[24)] Conductive materials are helpful as transductive materials for rapid electron transfer at the electrocatalyst–electrode interface.[25)] Graphene, a two-dimensional sp^2 bonded carbon substance with a honeycomb structure, is used widely as a catalyst because of its good features, including its large surface area, high conductivity, and biocompatibility.[26)] The oxidation of graphite powder produces graphene oxide (GO). The reduction of GO is called reduced graphene oxide (rGO).[27),28)] Actually, GO contains oxygen-containing functional groups, making it less conductive than rGO and potentially increasing resistance.[22),29)] Its superior conductivity along with a large surface area and high electrocatalytic activity makes rGO a potential candidate for AA electrooxidation.[30)] Earlier studies have demonstrated that rGO has outstanding catalytic activity for AA electrooxidation with low oxidation potential and higher current response.[30),31)] Previous studies showed different types of carbon materials showed good performance both in acidic and alkaline membrane based AA based fuel cells.[15),17),19)] Vulcan carbon exhibited the best performance (158 mW cm^{-2}) using a split pH (cation exchange) based AA fuel cell. [32)] Therefore, developing alternative carbon catalysts like rGO could open a new opportunity to enhance AA catalytic performance.

Several methods for synthesizing rGO from GO, including chemical, thermal, and hydrothermal procedures have been reported.[30),33),34)] The chemical reduction process provides several benefits including excellent stability, economic effectiveness, and a shorter manufacturing time.[35)] However, agglomeration of rGO results in decreasing electrical performance and exhibits low surface area.[36)] For catalytic performance, the stacking effect of graphene sheets has proved crucially important. Multiwall carbon nanotubes (MWCNTs), which are often used to enhance electrocatalytic performance, have excellent mechanical properties, high surface area, and chemical stability.[37)] Moreover, MWCNTs are widely recognized for their ability to bond with rGO through van der Waals forces and hydrogen bonds. Consequently, MWCNTs might be used as a spacer between

interfacial graphene layers during the reduction of rGO, thereby preventing agglomeration and increasing the specific surface area for electrocatalysis.[36),38)] The combination of rGO with MWCNT catalyst demonstrated excellent electrocatalytic activity for AA oxidation.[25)] So the rGO and the MWCNT could be used as alternative carbon materials for the AA oxidation.

To enhance the catalytic efficiencies of rGO and MWCNT nanocomposites further, researchers have added metal nanoparticles (NPs).[33),36),39)–41)] Of them, Pt and Pd metals are the most promising candidates for anode catalysts in energy conversion and storage devices because of their superior electrocatalytic efficacy.[42)–44)] However, Pd-based anode catalyst shows higher performance than Pt in the electrocatalytic oxidation of AA.[45)–47)] The Pd catalyst exhibits best AA-based fuel cell performance than the Pt catalyst.[48)] Therefore, the combination of Pd NPs with rGO and MWCNTs hybrid nanocomposite might enhance AA electrooxidation. This report is the first to describe a study of the combination of Pd NPs with rGO and MWCNT for AA electrooxidation.

Numerous studies have examined the inclusion of Pd NPs in a hybrid nanocomposite of rGO and MWCNT.[33),39),40),45),49),50)] Furthermore, one-pot synthesis of the chemical reduction method is preferable for a simple and shorter preparation time. For this study, a one-pot chemical reduction process was developed to prepare Pd NPs incorporated rGO and MWCNT hybrid nanocomposite (Pd/rGO/MWCNT) for AA electrooxidation, with the application as an anode catalyst for the AA-based DLFCs system. An earlier study demonstrated that the direct alkaline AA-based DLFCs (DAAFC) performed better than in acidic conditions.[32)] Recent studies showed the high performance of the DAAFC by using Pd and carbon-based catalysts.[15),32),51)] The excellent performance of AA-based fuel cells is comparable to that of alcohol-based fuel cells.[32)] This will help to construct an environmentally beneficial energy conversion system which is a barrier for alcohol-based fuel cells due to CO_2 emissions. Therefore, we concentrated on the improvement of the AA oxidation by introducing Pd NPs with rGO and MWCNT carbon materials. We have studied the electrochemical performance of a hybrid nanocomposite for AA electrooxidation in alkaline condition.

2. Experimental methods

2.1 Chemicals and Instruments

Analytical grade MWCNT (20–30 nm), AA, sodium tetrachloropalladate (II) (Na_2PdCl_4), 5% Nafion solution, sodium borohydride ($NaBH_4$), sulfuric acid (H_2SO_4), and potassium hydroxide (KOH) were purchased and used as received from Fujifilm Wako Pure Chemical Corp. The GO was purchased from NiSiNa Materials Co. Milli-Q water was used to prepare all the necessary solutions.

2.2 Synthesis of the Nanocomposite

Pd/rGO/MWCNT, Pd/rGO, and rGO/MWCNT catalysts were prepared using a chemical reduction technique with $NaBH_4$ as the reductant. To prepare Pd/rGO/MWCNT, 20 mg GO and 20 mg MWCNT were dispersed ultrasonically in 20 mL of deionized water. Subsequently, 5.0 mL of 15 mM Na_2PdCl_4 solution (dissolved in 0.1 M H_2SO_4) was added. The solution was then treated ultrasonically for another 30 min. Gradually and dropwise, 7.6 mL of freshly prepared 0.5 M $NaBH_4$ was added to the reactant to produce a solution pH 10. The reactant was then agitated at room temperature for 4 h. The catalyst was then filtered using filter paper and was rinsed three times with deionized water and ethanol. Finally, the catalyst was dried in a vacuum oven at 30 °C (12 h). The other two catalysts were prepared in the same manner as described above, but only metal precursor and GO were added to Pd/rGO. For rGO/MWCNT, no metal precursor was added.

2.3 Characterization

Field-emission scanning electron microscopy (FE-SEM, S4100; Hitachi Ltd.) and scanning electron microscopy (SEM) combined with energy-dispersive X-ray spectroscopy (EDX, TM3030Plus miniscope; Hitachi Ltd.) were used to describe the morphology of the as-prepared catalysts. To ascertain the elemental composition, XPS measurement was done using a delay-line detector (DLD) spectrometer (Kratos Axis-Ultra; Kratos Analytical Ltd.) equipped with an Al K radiation source (1486.6 eV). The size of Pd NPs was ascertained using transmission electron microscopy (TEM) (H-7100; Hitachi Ltd.). Powder X-ray diffractometer (XRD) patterns were acquired using a completely automated horizontal multipurpose X-ray diffractometer (Rigaku Smartlab; Rigaku Corp.) with a 2θ range of 20° to 90°. Brunauer–Emmett–Teller (BET) technique was used to determine the surface area of the catalysts using BELSORP-mini II-BP. All electrochemical measurements were

performed using a CHI 701 potentiostat equipped with a three-electrode setup. The working electrode, reference electrode, and counter electrode were GCE (3 mm diameter), Ag/AgCl (sat. KCl), and Pt wire, respectively.

2.4 Preparation of Pd/rGO/MWCNT/GCE

The GCE surface was cleaned by rubbing alumina powder (0.05 μm diameter) and was then sonicated with ethanol and water for 10 min to remove contaminants. The GCE surface was then cleaned electrochemically by potential cycling from 0 to +1.0 V at a scan rate of 100 mV s^{-1} in 0.1 M H_2SO_4 (Ar saturated) and was allowed to dry at ambient temperature. Then the GCE was modified with a suspension of a catalyst to investigate AA electrooxidation. To begin, the catalyst ink solution was prepared by dispersion of 2 mg Pd/rGO/MWCNT in 200 μL of 0.25% Nafion–ethanol solution, followed by ultrasonication for a homogeneous mixture. Then, a catalyst ink solution containing 0.04 mg Pd was dripped over the clean GCE surface and was allowed to dry at room temperature. The modified electrode was designated as Pd/rGO/MWCNT/GCE, whereas Pd/rGO/GCE and rGO/MWCNT/GCE were used respectively to refer to Pd/rGO and rGO/MWCNT. Fig.1 comprehensively presents the preparation of Pd/rGO/MWCNT/GCE. All the electrochemical studies were conducted in an alkaline environment with deaeration at room temperature (25 °C ± 0.5 °C).

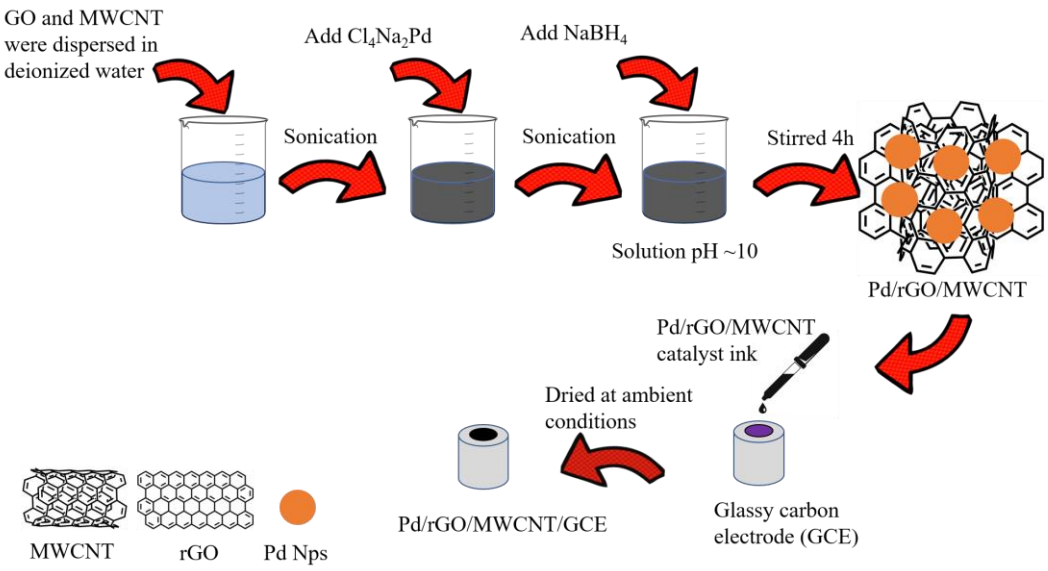

Fig. 1. Preparation of Pd/rGO/MWCNT/GCE and deposition to the GCE.

3. Results and discussion

3.1 Morphological and elemental analyses

The field-emission scanning electron microscopy (FE-SEM) image of the Pd/rGO/MWCNT composite is portrayed in Fig. 2a. Fig. 2b presents a high-magnification image of one portion of the Pd/rGO/MWCNT composite. The wrinkles in the image suggest that the chemical reduction process successfully produced rGO from GO.[25)] Fig. S1 shows FE-SEM images of GO, Pd/rGO, and rGO/MWCNT. Compared to the GO, all synthesized materials had completely different surface morphology. The change in the morphology further proved the successful reduction of GO by the chemical reduction process. Fig. 2c shows a scanning electron microscopy (SEM) image of Pd/rGO/MWCNT for energy-dispersive X-ray spectroscopy (EDX) analysis. Because of the presence of Pd metal, bright spots appear. A similar observation was made in the case of Pd/rGO (Fig. S1c). Fig. 2d–f respectively portray the elemental mapping of C, O, and Pd. Elemental mapping demonstrated a uniform distribution of Pd metal across the rGO and MWCNT systems. Fig. 2g shows elemental spectra of the Pd/rGO/MWCNT, which also revealed the existence of Pd. A trace amount of oxygen is detected in the EDX mapping because of Pd metal oxidation, which is also found in the XPS study. The rGO still contains a trace amount of oxygen in addition to Pd metal oxidation.

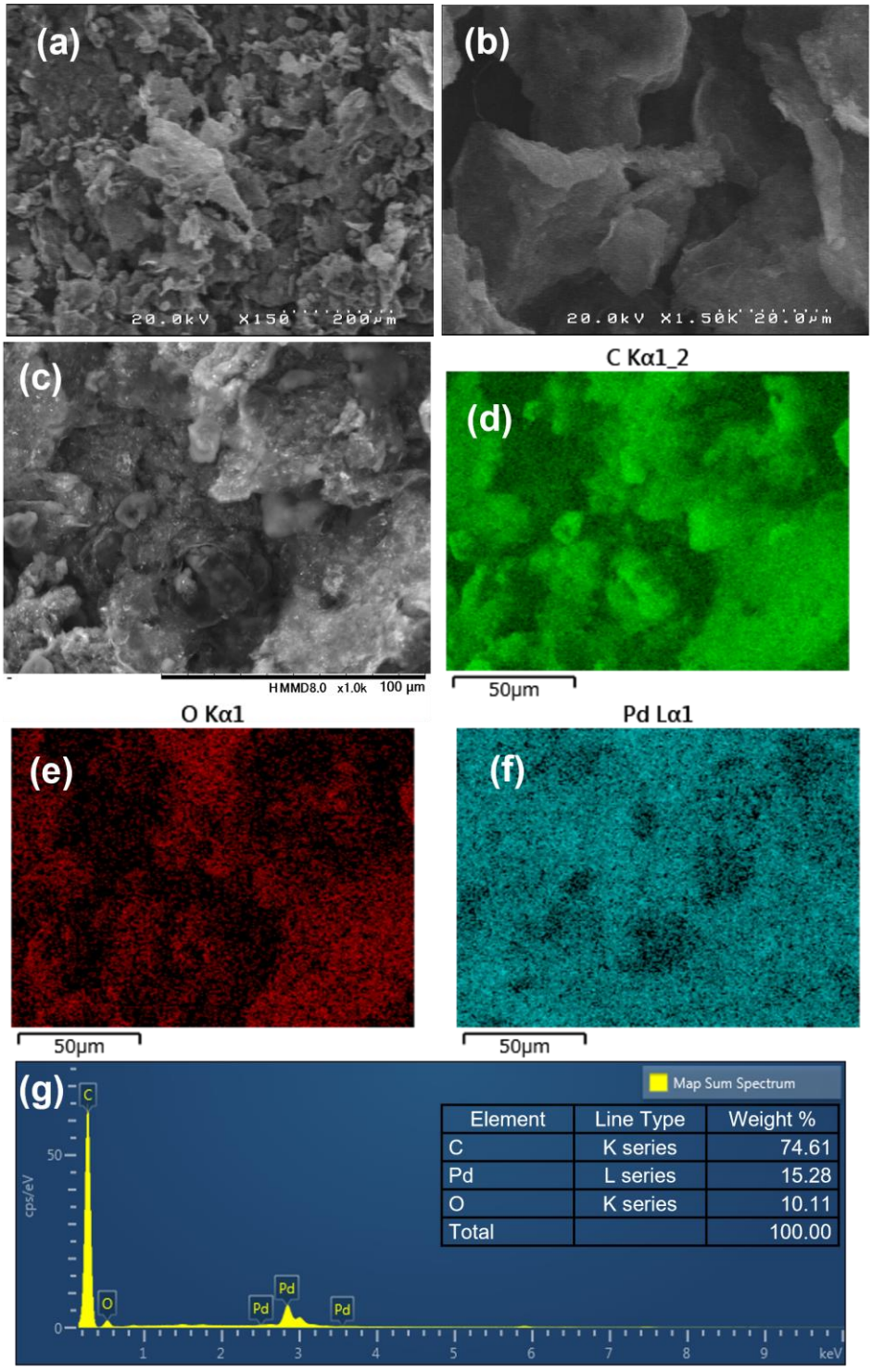

Fig. 2. Morphological and elemental characterization of Pd/rGO/MWCNT. (a) Low magnification and (b) high magnification FE-SEM image; (c) SEM image for EDX analysis, elemental mapping of (d) C, (e) O, (f) Pd, and (g) elemental spectra (inset table: element weight ratio).

Fig. 3a shows X-ray powder diffraction (XRD) patterns that confirm the Pd diffraction peaks and the carbon peaks. The diffraction patterns of all Pd-containing catalysts are comparable. The Pd (111) plane corresponds to the diffraction peak at 40.1°.[52),53)] Both Pd/rGO/MWCNT and rGO/MWCNT have peaks at 25.8° corresponding to the C (002) plane to an interlayer spacing of 3.45 Å.[54)–56)] The broad diffraction peak of the C (002) plane in Pd/rGO is attributable to the lesser degree of agglomeration of the rGO sheets.[57)] Next, the oxidation state of carbon and Pd metals was determined via X-ray photoelectron spectroscopy (XPS) analysis (Fig. 3b and c). XPS is an effective tool for verifying the successful reduction of GO because the oxo groups in the C 1s XPS spectra will be reduced in the presence of rGO. Fig. S2a shows C 1s XPS data from the GO. For GO, the deconvoluted C 1s showed the existence of C–C, C–O, and C=O, with the respective binding energies of 284.5 eV, 286.6 eV, and 288.2 eV.[58),59)] The deconvoluted C 1s peak of Pd/rGO/MWCNT is shown in Fig. 3b, where the C–O signal is markedly weaker, and where the C=O peak is very low, showing effective GO reduction.[58)] Fig. S2b and Fig. S2c show similar features in deconvoluted C 1s spectra of rGO/MWCNT and Pd/rGO, respectively. This finding indicates that the GO was reduced by chemical reduction in all cases. The peak attributable to π–π* interaction was discovered at binding energy 291.1 eV in both Pd/rGO/MWCNT (Fig. 3b) and Pd/rGO (Fig. S2c).[58)] The Pd 3d XPS spectra of Pd/rGO/MWCNT are portrayed in Fig. 3c. With a 5.2 eV gap, two peaks were found with binding energies of 340.8 eV and 335.6 eV for Pd ($3d_{3/2}$) and Pd ($3d_{5/2}$).[34),39),41),52),58)] According to XPS measurements, Pd NPs were in a metallic state in Pd/rGO/MWCNT. The chemical reduction process converts Pd precursor to metal Pd. From XPS data, a small amount of PdO was discovered with higher binding energy than metal Pd. In Pd/rGO, the Pd 3d XPS spectra exhibited similar features to the Pd/rGO/MWCNT (Fig. S2d). The Pd 3d XPS data of Pd/rGO also demonstrated Pd NPs are in metallic states. The Pd NPs were examined next using transmission electron microscopy (TEM). Fig. 3d presents a TEM picture of Pd/rGO/MWCNT. The Pd NPs are dispersed on the rGO/MWCNT support. According to the inset histogram, the average size of the Pd NPs is roughly 9 nm. The TEM image shows the Pd NPs as spherical.

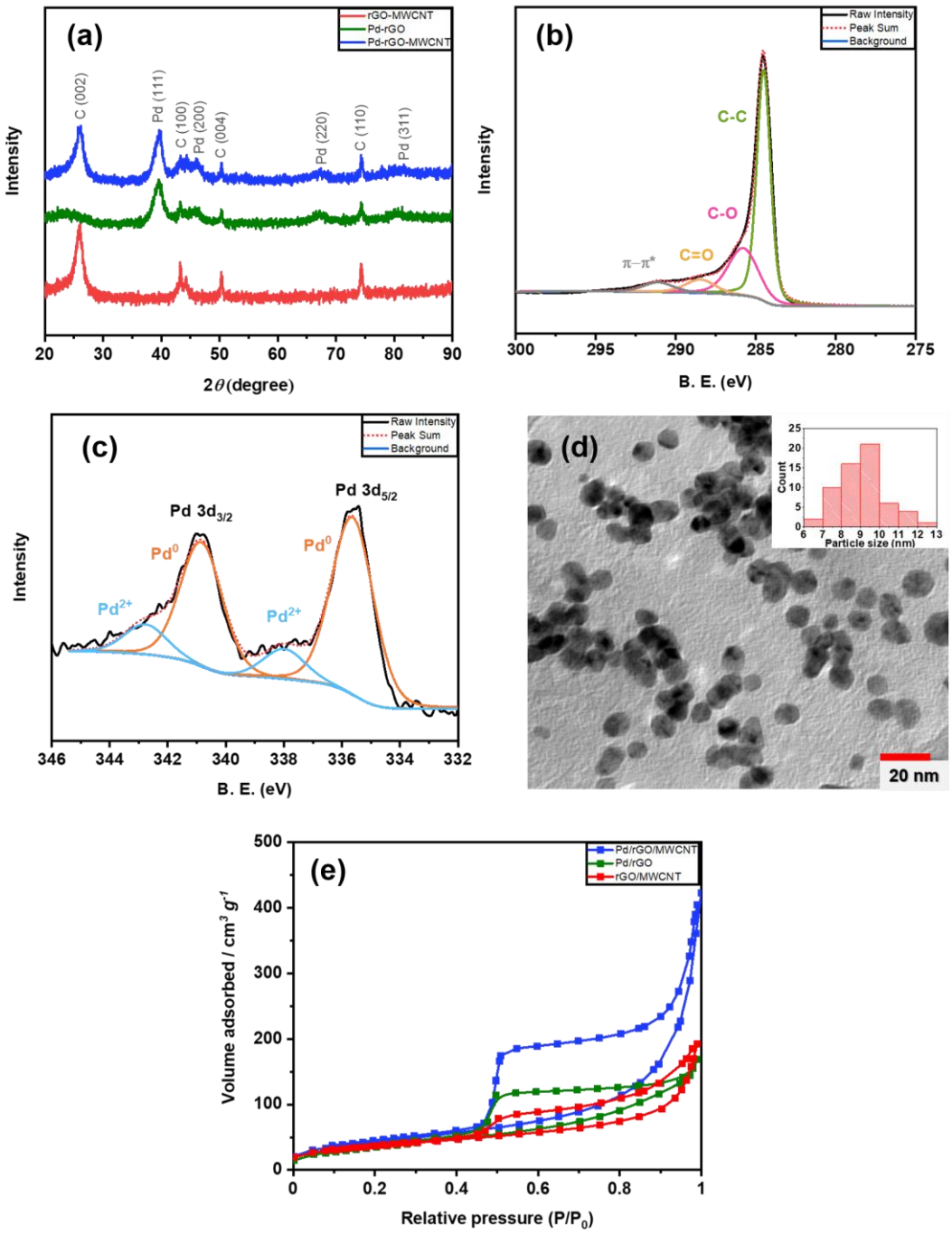

Fig. 3. (a) XRD patterns of as-synthesized rGO/MWCNT, Pd/rGO, and Pd/rGO/MWCNT, with XPS spectra of Pd/rGO/MWCNT (b) C 1s and (c) Pd 3d. (d) TEM image of Pd/rGO/MWCNT (scale bar = 20 nm, inset: histogram of the Pd NPs). (e) Nitrogen adsorption–desorption curves of Pd/rGO/MWCNT, Pd/rGO and rGO/MWCNT.

As shown in Fig. 3e, the N_2 adsorption and desorption test (BET analysis) was conducted to analyze the surface area of all electrocatalysts. Table I presents the BET-specific surface area and total pore volume of all catalysts. The specific surface area of the Pd/rGO/MWCNT catalyst was higher than that of the Pd/rGO and rGO/MWCNT catalysts. The adsorption research results demonstrated that the pore volume of the Pd/rGO/MWCNT catalyst was similarly greater than that of the others. The inclusion of Pd and MWCNT between graphene layers enhanced the catalyst pore volume. When Pd and MWCNT are combined with rGO in Pd/rGO/MWCNT, the surface area, and pore volume increase in comparison to Pd/rGO and rGO/MWCNT individually. The synergistic effect of combining two complementary materials might enhance catalytic performance.

Table I. BET surface area and pore volume of Pd/rGO/MWCNT, Pd/rGO, and rGO/MWCNT

Catalyst	BET surface area ($m^2 g^{-1}$)	Pore volume ($cm^3 g^{-1}$)
Pd/rGO/MWCNT	153.7	0.61
Pd/rGO	130.1	0.26
rGO/MWCNT	130.7	0.29

3.2 Electrocatalytic performance

Cyclic voltammograms were obtained under various experimental conditions to investigate the electrocatalytic performance of Pd/rGO/MWCNT/GCE for the electrooxidation of AA molecules. In the presence of AA, the modified electrode response was evaluated, as shown in Fig. 4a. Cyclic voltammograms between -0.8 V and +0.7 V were obtained in the presence and absence of AA (5.6 mM) in 1 M KOH solution using Pd/rGO/MWCNT/GCE at a scan rate of 50 mV s^{-1}. A well-defined oxidation wave is generated by the oxidation of AA at -0.04 V, although no oxidation peak exists without AA. We also found an oxidation peak without the presence of AA at -0.15 V for the development of Pd^{2+} from Pd^0 under the alkaline condition.[52),60)] In our recent article we also observed the PdO peak in a similar potential for the Pd catalyst in the 1 M KOH solution.[52)] The peak potential of AA oxidation (-0.04 V) is more positive than the PdO peak (-0.15 V) as shown in Fig. 4a. The

reduction of PdO to Pd was attributed to a reduction peak detected at -0.5 V in 1 M KOH solution.[52] A large capacitive current is observed in Fig. 4a, which is very common for rGO/MWCNT systems.[25] The AA oxidation peak is further evaluated by the concentration-dependent study which is described in the later part.

We evaluate the electrocatalytic performance by comparing all catalyst electrodes to the bare GCE. Cyclic voltammograms of AA electrooxidation in an alkaline condition using the bare GCE and all modified electrodes are shown in Fig. 4b. We exclude the large capacitance current during electrocatalytic performance evaluation. We choose the potential range of AA oxidation for each catalyst and calculate the peak current density. The selected potential range for Pd/rGO/MWCNT/GCE is -0.20 V to +0.20 V and for Pd/rGO/GCE is -0.25 V to +0.25 V. The peak potential for AA oxidation is found at -0.04 V for Pd/rGO/MWCNT/GCE and Pd/rGO/GCE. The carbon catalysts also have catalytic activity for the AA oxidation as discussed in the introduction. The rGO/MWCNT and unmodified GCE showed low catalytic performance for AA oxidation. In Fig. 4b, rGO/MWCNT/GCE showed the AA oxidation peak at more negative potential with lower current density than other catalysts. In comparison to unmodified GCE and other catalysts, the Pd/rGO/MWCNT/GCE exhibits much higher catalytic activity for AA electrooxidation. The current density of the Pd/rGO/MWCNT/GCE (5.18 mA cm^{-2}) is higher than Pd/rGO/GCE (4.02 mA cm^{-2}), rGO/MWCNT/GCE (1.85 mA cm^{-2}) and bare GCE (0.6 mA cm^{-2}). This is due to the synergetic effect of Pd NPs with the rGO and MWCNT hybrid nanocomposite. The current increased significantly because of the increased surface area of the rGO and MWCNT hybrid nanocomposite. When Pd NPs are introduced into this hybrid nanocomposite, the electrocatalytic performance is improved considerably.

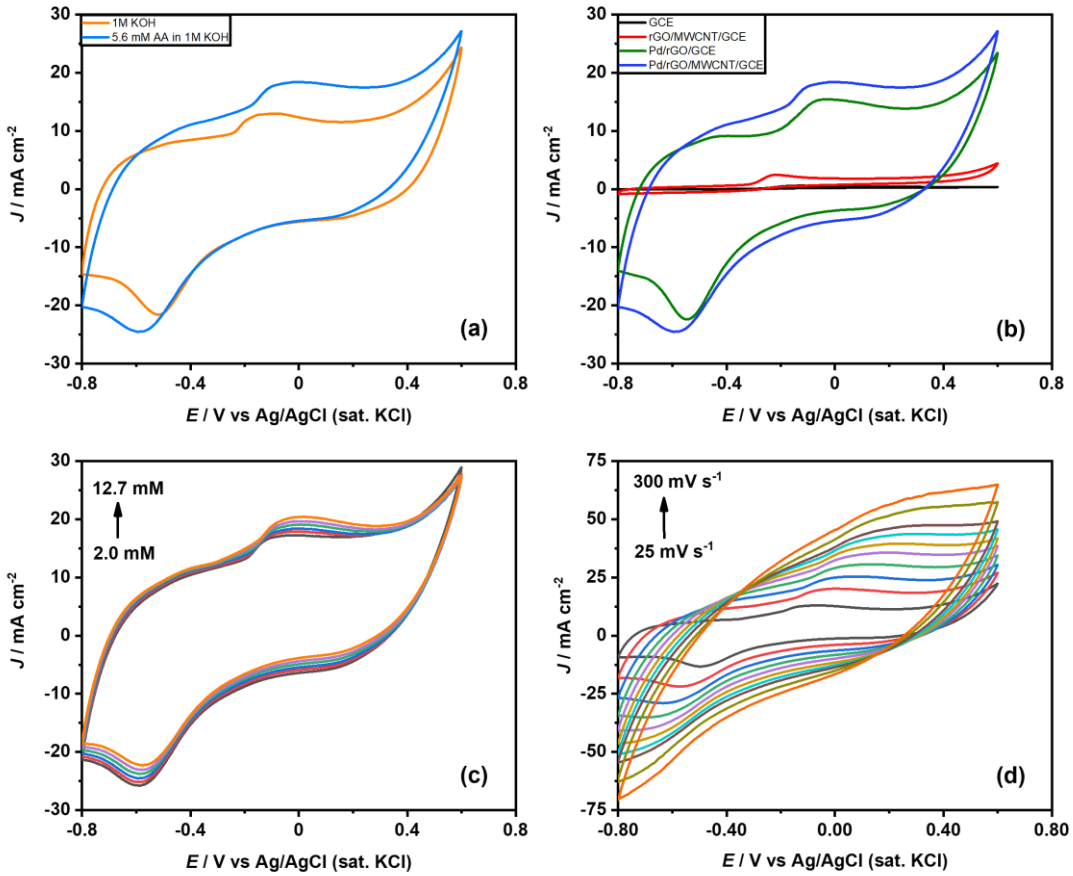

Fig. 4. (a) Cyclic voltammograms of Pd/rGO/MWCNT/GCE in the absence and presence of 5.6 mM ascorbic acid. (b) Catalytic activity comparison of bare GCE, rGO/MWCNT/GCE, Pd/rGO/GCE, and Pd/rGO/MWCNT/GCE for 5.6 mM ascorbic acid at 50 mV s^{-1}. (c) Concentration effect of ascorbic acid at 50 mV s^{-1}. (d) Scan rate effect of 12.7 mM ascorbic acid using Pd/rGO/MWCNT/GCE catalyst. All experiments described above were conducted in a 1 M KOH solution.

The electrochemically active surface area (ECSA) is investigated further to assess the electrochemical behavior of catalysts. The number of electrochemically active sites is described by the ECSA for metal catalyst mass. The ECSA of the two Pd catalysts (Pd/rGO/MWCNT/GCE and Pd/rGO/GCE) were calculated using the following equation.[52)]

$$\mathrm{ECSA} = Q/sl \qquad (1)$$

Here, Q represents the Coulombic charge of the PdO reduction peak (Fig. 4b); s denotes the proportionality constant =0.405 mC cm^{-2}. Also, l denotes the metal loading in g m^{-2}. Table II presents the ECSA values of prepared catalysts. The Pd/rGO/MWCNT/GCE catalyst showed the highest ECSA value. Therefore, the combination of Pd NPs with rGO and MWCNT enhanced the surface area for the electrocatalysis of AA oxidation. To evaluate electrocatalyst performance, we further checked the specific activity (SA) and mass activity (MA) for Pd/rGO/GCE and Pd/rGO/MWCNT/GCE towards AA oxidation in alkaline condition. The SA explains the inherent activity of the catalyst. The MA can be helpful in terms of commercial applications in which we can evaluate the activity of the catalyst per unit mass.[61] The SA is the current per unit ECSA of the catalyst. The SA is calculable from ECSA normalized catalytic current. The MA, the current per unit mass of the catalyst, is determined by the mass-normalized catalytic current.[61),62] The SA and MA values for Pd/rGO/MWCNT/GCE and Pd/rGO/GCE are also presented in Table II. The MA and the SA of Pd/rGO/MWCNT/GCE are around 1.6 and 1.1 times higher, respectively than those of Pd/rGO/GCE. The Pd/rGO/MWCNT/GCE also exhibits excellent electrocatalytic properties in terms of higher SA and MA for AA electrooxidation in alkaline condition.

Table II. Electrochemical characterizations for Pd/rGO/MWCNT/GCE and Pd/rGO catalyst in 5.6 mM AA + 1 M KOH solution

Catalyst	Metal loading (g m^{-2})	ECSA ($m^2 g^{-1}_{Pd}$)	MA (mA mg^{-1}_{Pd})	SA (mA cm^{-2})
Pd/rGO/MWCNT /GCE	6.7	10.5	7.8	0.074
Pd/rGO/GCE	8.0	7.2	5.0	0.069

Next, we evaluated the AA oxidation reaction process for the Pd/rGO/MWCNT/GCE.

At a scan rate of 50 mV s^{-1}, the concentration effect of AA on the Pd/rGO/MWCNT/GCE was explored further, with findings presented in Fig. 4c. The oxidation current increased as the concentration of AA increased. This finding indicates that the oxidation wave at -0.04 V is coming from the AA oxidation and the concentration of AA does not affect the Pd/rGO/MWCNT catalyst active site. The peak potential of AA

oxidation shifted positively as the concentration increased, indicating a diffusion-controlled process.[63] Interruption of the analyte mass transportation mechanism is responsible for this change. Current is explained by mass transfer from the bulk (solution) to the electrode surface. The increase in AA concentrations interrupts the diffusion process. The electrochemical system is more likely to restore mass transportation. As a result, the peak potential has shifted in a positive direction. If this oxidation wave is not coming from the AA oxidation, then the peak intensity as well as, peak shifting does not occur.

Fig. 4d presents the effects of scan rates on AA oxidation. The anodic peak current of Pd/rGO/MWCNT/GCE increased concomitantly with increasing scan rate, varying from 25 to 500 mV s^{-1}. To understand more about the scan rate influence on peak current behavior, we have conducted further research. The log peak current (I_p) versus log (scan rate) curve is shown in Fig. S3. The plots show a linear association with a slope of 0.49 (close to 0.5). The slope value indicates that, at the Pd/rGO/MWCNT/GCE surface, the solution to the electrode surface mass transfer step controls the AA oxidation.[20),52)]

Chronoamperometry was also used to elucidate the electrochemical stability of all catalysts.[64)] Stability assessment by chronoamperometry of Pd/rGO/MWCNT/GCE, Pd/rGO/GCE, and rGO/MWCNT/GCE electrodes is presented in Fig. 5, applying at -0.04 V potential of AA oxidation in 1 M KOH. After 1000 s, the current density of Pd/rGO/MWCNT/GCE is still higher than those of the other two catalysts. The stability of Pd/rGO/MWCNT/GCE for AA oxidation in the alkaline state is high. We inferred from these data that the Pd/rGO/MWCNT catalyst might be employed as an anode catalyst in alkaline AA fuel cells.

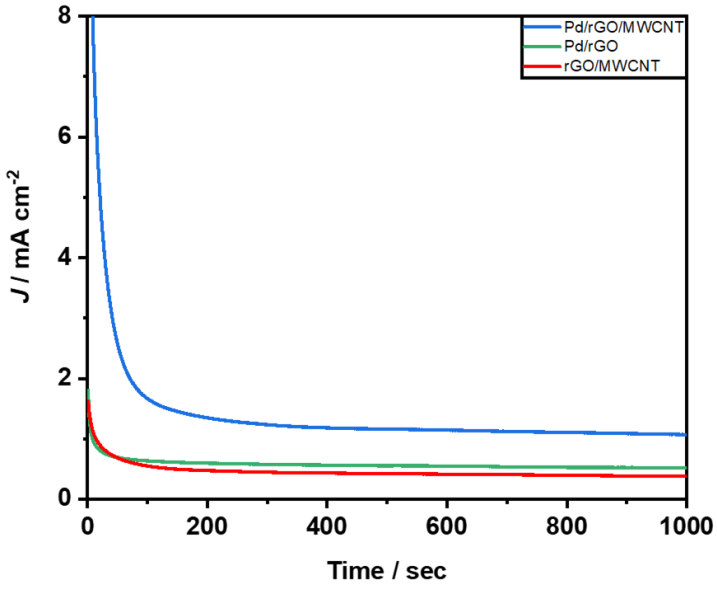

Fig. 5. Chronoamperometry of 5.6 mM ascorbic acid at rGO/MWCNT/GCE, Pd/rGO/GCE, and Pd/rGO/MWCNT/GCE.

The incorporation of Pd NPs into the rGO and MWCNT hybrid nanocomposite increases the electrochemical performance for AA electrooxidation considerably. Also, the Pd/rGO/MWCNT catalyst exhibits excellent stability for AA oxidation in the alkaline condition, promising candidate for AA based energy harvesting system.

4. Conclusions

After synthesizing Pd NPs incorporated rGO and MWCNT hybrid nanocomposite through a one-pot chemical reduction process, we used them for AA electrooxidation in the alkaline condition. Three modified electrodes were prepared using three synthesized catalysts. Pd/rGO/MWCNT/GCE showed better catalytic performance for AA electrooxidation compared to the other two modified electrodes (Pd/rGO/GCE and rGO/MWCNT/GCE). Additionally, the Pd/rGO/MWCNT/GCE demonstrated excellent stability to AA electrooxidation in an alkaline environment. The outstanding catalytic performance and suggest that Pd NPs with rGO and MWCNT, as an alternate carbon material, could be used for environmentally friendly energy harvesting systems.

Acknowledgments

Y. N. appreciated the support of JSPS KAKENHI grant numbers JP21H00020, The Murata Science Foundation, and JST CREST Grant Number JPMJCR21B3, Japan. We are grateful to Professor Tsuyohiko Fujigaya of Kyushu University in Japan for his helpful scientific discussion.

Appendix

Supplementary data

Surface area calculation; SEM, XPS study of GO, rGO/MWCNT, Pd/rGO; Log (Ip) vs. log (scan rate) plots of Pd/rGO/MWCNT.

ORCID

Md. M. Hasan: https://orcid.org/0000-0001-5617-100X

Y. Nagao: https://orcid.org/0000-0003-1249-440X

Z. Li: https://orcid.org/0000-0002-0146-5526

Conflicts of interest

There are no conflicts to declare. No author has any competing financial interest related to this report or the study it describes.

References

1) E. Mourad, L. Coustan, P. Lannelongue, D. Zigah, A. Mehdi, A. Vioux, S. A. Freunberger, F. Favier and O. Fontaine, Nat. Mater. **16** [4], 446 (2017).

2) N. Mahne, B. Schafzahl, C. Leypold, M. Leypold, S. Grumm, A. Leitgeb, G. A. Strohmeier, M. Wilkening, O. Fontaine, D. Kramer, C. Slugovc, S. M. Borisov and S. A. Freunberger, Nat. Energy **2** [5], 1 (2017).

3) Y. Nabil, S. Cavaliere, I. A. Harkness, J. D. B. Sharman, D. J. Jones and J. Rozière, J. Power Sources **363**, 20 (2017).

4) S. Nanda, R. Rana, Y. Zheng, J. A. Kozinski and A. K. Dalai, Sustain. Energy Fuels **1** [6], 1232 (2017).

5) M. del Cueto, P. Ocón and J. M. L. Poyato, J. Phys. Chem. C **119** [4], 2004 (2015).
6) S. Goodwin and D. A. Walsh, ACS Appl. Mater. Interfaces **9** [28], 23654 (2017).
7) T. B. Ferriday and P. H. Middleton, Int. J. Hydrogen Energy **46** [35], 18489 (2021).
8) A. Mahajan, S. Banik, D. Majumdar and S. K. Bhattacharya, ACS Omega **4** [3], 4658 (2019).
9) L. An and R. Chen, J. Power Sources **329**, 484 (2016).
10) Z. Tao, Q. Zhang, X. Xi, G. Hou and L. Bi, Electrochem. commun. **72**, 19 (2016).
11) J. Ma, N. A. Choudhury and Y. Sahai, Renew. Sustain. Energy Rev. **14** [1], 183 (2010).
12) J. Sanabria-Chinchilla, K. Asazawa, T. Sakamoto, K. Yamada, H. Tanaka and P. Strasser, J. Am. Chem. Soc. **133** [14], 5425 (2011).
13) D. Sebastián, A. Serov, I. Matanovic, K. Artyushkova, P. Atanassov, A. S. Aricò and V. Baglio, Nano Energy **34** [February], 195 (2017).
14) D. K. Ross, Vacuum **80** [10], 1084 (2006).
15) O. Muneeb, E. Do, T. Tran, D. Boyd, M. Huynh, G. Ghosn and J. L. Haan, J. Power Sources **351**, 74 (2017).
16) B. R. Sathe, J. Electroanal. Chem. **799** [January], 609 (2017).
17) M. Choun, H. J. Lee and J. Lee, J. Energy Chem. **25** [5], 793 (2016).
18) S. Uhm, J. Choi, S. T. Chung and J. Lee, Electrochim. Acta **53** [4], 1731 (2007).
19) N. Fujiwara, S. Yamazaki, Z. Siroma, T. Ioroi and K. Yasuda, J. Power Sources **167** [1], 32 (2007).
20) M. M. Hasan, R. H. Rakib, M. A. Hasnat and Y. Nagao, ACS Appl. Energy Mater. **3** [3], 2907 (2020).
21) S. Kuss and R. G. Compton, Electrochim. Acta **242**, 19 (2017).
22) Y. Zhao, J. Qin, H. Xu, S. Gao, T. Jiang, S. Zhang and J. Jin, Microchim. Acta **186** [1], 17 (2019).
23) C. L. Sun, C. T. Chang, H. H. Lee, J. Zhou, J. Wang, T. K. Sham and W. F. Pong, ACS Nano **5** [10], 7788 (2011).
24) J. N. Tiwari, V. Vij, K. C. Kemp and K. S. Kim, ACS Nano **10** [1], 46 (2016).
25) M. A. Zahed, S. C. Barman, R. M. Toyabur, M. Sharifuzzaman, X. Xuan, J. Nah and J. Y. Park, J. Electrochem. Soc. **166** [6], B304 (2019).

26) H. Bagheri, A. Hajian, M. Rezaei and A. Shirzadmehr, J. Hazard. Mater. **324**, 762 (2017).

27) B. Gadgil, P. Damlin and C. Kvarnström, Carbon N. Y. **96**, 377 (2016).

28) S. Kellici, J. Acord, J. Ball, H. S. Reehal, D. Morgan and B. Saha, RSC Adv. **4** [29], 14858 (2014).

29) H. Xu, Q. Li, L. Wang, Y. He, J. Shi, B. Tang and C. Fan, Chem. Soc. Rev. **43** [8], 2650 (2014).

30) J. Jiang and X. Du, Nanoscale **6** [19], 11303 (2014).

31) L. Yang, D. Liu, J. Huang and T. You, Sensors Actuators B Chem. **193**, 166 (2014).

32) O. Muneeb, I. Chino, A. Saenz and J. L. Haan, J. Power Sources **413**, 216 (2019).

33) S. Tourani, A. M. Rashidi, A. A. Safekordi, H. R. Aghabozorg and F. Khorasheh, Ind. Eng. Chem. Res. **54** [31], 7591 (2015).

34) H. Ye, Y. Li, J. Chen, J. Sheng, X. Z. Fu, R. Sun and C. P. Wong, J. Mater. Sci. **53** [23], 15871 (2018).

35) M. Abu Zahed, S. C. Barman, M. Sharifuzzaman, X. Xuan, J. S. Nah and J. Y. Park, J. Electrochem. Soc. **165** [16], B840 (2018).

36) Z. Li, X. Dai, K. Du, Y. Ma, M. Liu, H. Sun, X. Ma and X. Zhang, J. Phys. Chem. C **120** [3], 1478 (2016).

37) D. E. Bayraktepe, Z. Yazan and M. Önal, Talanta **203** [February], 131 (2019).

38) X. Jiang, Y. Wu, X. Mao, X. Cui and L. Zhu, Sensors Actuators B Chem. **153** [1], 158 (2011).

39) A. Bin Yousaf, M. Imran, A. Zeb, X. Xie, K. Liang, X. Zhou, C. Z. Yuan and A. W. Xu, Catal. Sci. Technol. **6** [13], 4794 (2016).

40) J. Hu, Z. Zhao, J. Zhang, G. Li, P. Li, W. Zhang and K. Lian, Appl. Surf. Sci. **396**, 523 (2017).

41) T. Sun, Z. Zhang, J. Xiao, C. Chen, F. Xiao, S. Wang and Y. Liu, Sci. Rep. **3** [1], 2527 (2013).

42) D. Larcher and J.-M. Tarascon, Nat. Chem. **7** [1], 19 (2015).

43) I. E. L. Stephens, J. Rossmeisl and I. Chorkendorff, Science (80-.). **354** [6318], 1378 (2016).

44) H. Huang, S. Yang, R. Vajtai, X. Wang and P. M. Ajayan, Adv. Mater. **26** [30], 5160

(2014).

45) F. Yang, J. Wang, Y. Cao, L. Zhang and X. Zhang, Sensors Actuators B Chem. **205**, 20 (2014).

46) G. Wu, Y. Wu, X. Liu, M. Rong, X. Chen and X. Chen, Anal. Chim. Acta **745**, 33 (2012).

47) X. Zhang, Y. Cao, S. Yu, F. Yang and P. Xi, Biosens. Bioelectron. **44** [1], 183 (2013).

48) N. Fujiwara, K. Yasuda, T. Ioroi, Z. Siroma, Y. Miyazaki and T. Kobayashi, Electrochem. Solid-State Lett. **6** [12], A257 (2003).

49) A. Uzunoglu, D. A. Kose, E. Gokmese and F. Gokmese, J. Clust. Sci. **31**, 231 (2020).

50) D. Rajesh, P. Indra Neel, A. Pandurangan and C. Mahendiran, Appl. Surf. Sci. **442**, 787 (2018).

51) O. Muneeb, E. Do, D. Boyd, J. Perez and J. L. Haan, Appl. Energy **235**, 473 (2019).

52) M. M. Hasan and Y. Nagao, ChemistrySelect **6** [24], 5885 (2021).

53) C. Lu, W. Guan, T. K. A. Hoang, Y. Li, T. N. L. Doan and H. Zhao, Int. J. Electrochem. Sci. **10** [6], 5077 (2015).

54) C. Luhrs, M. Moberg, A. Maxson, L. Brewer and S. Menon, Inorganics **2** [2], 211 (2014).

55) F. Du, J. Yuan, M. Zhang, J. Li, Z. Zhou, Z. Li, M. Cao, J. Chen, L. Zhang, X. Liu, A. Gong, W. Xu and Q. Shao, RSC Adv. **4** [71], 37536 (2014).

56) N. Jha, P. Ramesh, E. Bekyarova, M. E. Itkis and R. C. Haddon, Adv. Energy Mater. **2** [4], 438 (2012).

57) P. K. Sahoo, B. Panigrahy, D. Li and D. Bahadur, J. Appl. Phys. **113** [17], 17B525 (2013).

58) Y. She, Z. Lu, W. Fan, S. Jewell and M. K. H. Leung, J. Mater. Chem. A **2** [11], 3894 (2014).

59) K. V. Sankar, R. K. Selvan, R. H. Vignesh and Y. S. Lee, RSC Adv. **6** [72], 67898 (2016).

60) B. Habibi and S. Mohammadyari, Int. J. Hydrogen Energy **40** [34], 10833 (2015).

61) M. D. Obradović, Z. M. Stančić, U. Č. Lačnjevac, V. V. Radmilović, A. Gavrilović-Wohlmuther, V. R. Radmilović and S. L. Gojković, Appl. Catal. B

Environ. **189**, 110 (2016).

62) M. Li, K. Duanmu, C. Wan, T. Cheng, L. Zhang, S. Dai, W. Chen, Z. Zhao, P. Li, H. Fei, Y. Zhu, R. Yu, J. Luo, K. Zang, Z. Lin, M. Ding, J. Huang, H. Sun, J. Guo, X. Pan, W. A. Goddard, P. Sautet, Y. Huang and X. Duan, Nat. Catal. **2** [6], 495 (2019).

63) M. A. Hasnat, M. M. Hasan, N. Tanjila, M. M. Alam and M. M. Rahman, Electrochim. Acta **225**, 105 (2017).

64) D. F. Silva, A. O. Neto, E. S. Pino, M. Linardi and E. V. Spinacé, in *Studies in Surface Science and Catalysis* (2010) Vol. 175 pp. 555.